

Smart Thermally Actuating Textiles

Vanessa Sanchez, Christopher J. Payne, Daniel J. Preston, Jonathan T. Alvarez, James C. Weaver, Asli T. Atalay, Mustafa Boyvat, Daniel M. Vogt, Robert J. Wood, George M. Whitesides, and Conor J. Walsh*

Soft robots have attracted attention for biomedical and consumer devices. However, most of these robots are pneumatically actuated, requiring a tether and thus limiting wearable applications that require multiple controlled actuators. By pairing liquid-vapor phase change actuation with a textile-based laminated manufacturing method, smart thermally actuating textiles (STATs) eliminate the need for a pneumatic tether. STATs are lightweight and unobtrusive for wearable applications and exploit a facile manufacturing approach that supports arbitrary customization of the form factor and easy creation of connected arrays of individual robotic modules. Through integrated sensing and heating elements, STATs demonstrate closed-loop feedback that enables dynamic pressure control in the presence of environmental temperature fluctuations.

1. Introduction

Biologically inspired actuators made from soft materials are innately compliant, adaptable to their environment, and able to perform biomimetic motions;^[1–4] as such, they are ideal for devices that interact with humans, including wearable robots.^[5–7] The majority of current soft robots rely on a pressurized fluid delivered via tether and require hardware (e.g., pumps and valves) to supply the fluid and control its flow. This hardware, which can often be heavy, noisy, and bulky,^[1,2] prevents the realization of lightweight and portable wearable devices, especially for applications requiring multiple actuator arrays because the number of valves and pneumatic lines scales with the number of

actuators. This can pose a challenge for the development of soft robotic devices that require multiple controlled actuators, such as wearable robots to assist multiple-degree-of-freedom limb movement for assistance^[7] or rehabilitation^[6] or active pressure modulation devices for prevention of pressure sores or mechanotherapy applications.^[8]

To remove the need for a pressurized fluid supply, researchers have developed alternative electrically and thermally activated soft actuator technologies including shape memory polymers,^[9,10] piezopolymers,^[11] electrostatic actuators,^[12,13] charge-injection electrohydrodynamic devices,^[14] electrolysis-based actuators,^[15] and encapsulated electromagnetic systems.^[16] Building upon this work, researchers have translated untethered soft actuator designs to textiles when considering wearable applications, motivated by the prevalence of textiles as the base material for the vast majority of soft goods and clothing. Every day we intimately interact with textiles because they are lightweight, conformal (compared to molded and printed elastomeric systems), and robust to repeated, sometimes violent, stresses and abrasions encountered during use (compared to polymer films).

The hierarchical nature of textiles provides the opportunity to create soft robotic systems for wearable devices through the integration of smart fibers that can sense or actuate by electrical or chemical means.^[17,18] Textile systems that can apply force, change shape, or modulate stiffness have been achieved through the integration of shape-memory alloys (SMAs) as fibers into the textile structure.^[19,20] Other textile actuation approaches include thermally actuated coiled

V. Sanchez, Dr. C. J. Payne, J. T. Alvarez, Prof. A. T. Atalay, Dr. M. Boyvat, D. M. Vogt, Prof. R. J. Wood, Prof. C. J. Walsh
John A. Paulson School of Engineering and Applied Sciences
Harvard University
29 Oxford Street, Cambridge, MA 02138, USA
E-mail: walsh@seas.harvard.edu


V. Sanchez, Dr. C. J. Payne, Prof. D. J. Preston, J. T. Alvarez, Dr. J. C. Weaver, Prof. A. T. Atalay, Dr. M. Boyvat, D. M. Vogt, Prof. R. J. Wood, Prof. G. M. Whitesides, Prof. C. J. Walsh
Wyss Institute for Biologically Inspired Engineering
Harvard University
3 Blackfan Circle, Boston, MA 02115, USA

V. Sanchez, Prof. D. J. Preston, Prof. G. M. Whitesides
Department of Chemistry and Chemical Biology
Harvard University
12 Oxford Street, Cambridge, MA 02138, USA

Prof. D. J. Preston
Department of Mechanical Engineering
Rice University
6100 Main Street, Houston, TX 77005, USA

Prof. A. T. Atalay
Department of Textile Engineering
Faculty of Technology
Marmara University
Göztepe Kampüsü, Kadıköy, Istanbul 34722, Turkey

Prof. G. M. Whitesides
Kavli Institute for Bionano Science and Technology
Harvard University
29 Oxford Street, Cambridge, MA 02138, USA

 The ORCID identification number(s) for the author(s) of this article can be found under <https://doi.org/10.1002/admt.202000383>.

DOI: 10.1002/admt.202000383

fibers^[21,22] and electrochemically actuated fibers^[23] as artificial muscles. Smart fibers have utilized capacitive,^[24–26] resistive,^[27–29] and optical^[30,31] principles to sense bending, torsion, pressure, and strain. While closed-loop control has not yet been demonstrated, textile systems that incorporate both actuating and sensing elements are beginning to emerge. Specific implementations include SMA-based textile systems with integrated soft strain sensors for motion tracking^[32] and elastomer fibers coated with electrically conductive carbon nanotubes to enable thermal actuation and resistive strain sensing.^[33] These approaches have the advantage of a form factor that integrates with textile manufacturing equipment (e.g., knitting machines and weaving looms), but this benefit also comes at a cost—the machinery is specialized, and its operation and programming requires specific technical expertise,^[34] resulting in methods for textile-integrated wearable and soft robotic device development that are inaccessible to most roboticists.

For wearable device applications that do not require high bandwidth (e.g., delivering controlled sequential compression in mechanotherapy), phase change actuators are a promising new technology that may provide a suitable approach because they can provide high forces and strains, in terms of volumetric expansion, at low voltages over many cycles.^[35] These actuators incorporate cavities containing volatile fluids, such as alcohols or fluorocarbons,^[35–42] which exhibit large changes in vapor pressure upon adding only small inputs of power, enabling significant increases in pressure in each cavity when power is applied. This approach initially gained traction using molded and printed elastomeric actuators, which are nonplanar in their unactuated state,^[35] but is amenable to a variety of other material architectures, including initially flat pouches made from films^[39] or textiles, which may be more suitable for wearable systems. A further advantage of using textiles for heating is that commercially available textile sheets can be readily modified with either printing^[37] or laser cutting technologies.^[43] Such batch production techniques can enable the development of complex, multiactuator devices^[44,45] and allow customization for specific wearable applications.

In order to develop phase change actuators for wearable systems, several key considerations and challenges must be addressed. First, phase change actuators exhibit limited controllability in unknown environments. Prior work has illustrated that ambient thermal conditions greatly affect phase change actuator performance,^[37] and only binary actuation (i.e., inflated vs deflated) has been achieved reliably across different environmental conditions.^[41] This limited controllability prevents the translation of phase change actuators to wearable applications which commonly require controlled actuation in temporally dependent motion profiles within environments as varied and uncertain as those encountered by the wearer. Second, low profile, robust, and completely soft approaches for encapsulating the working fluid remain limited: current elastomer-based approaches are often bulky, while films are subject to failure after repeated bending. Finally, manufacturing methods readily accessible to roboticists that enable rapid prototyping of textile-based heaters and pressure sensing elements that can be easily integrated together do not exist.

2. STAT Overview and Fabrication

To overcome these challenges, we present smart thermally actuating textiles (STATs), soft robotic textiles that combine phase change actuation with integrated sensing and closed-loop feedback control that can be rapidly customized and prototyped using accessible equipment (**Figure 1**). Each STAT textile pouch encapsulates a methoxy-fluorocarbon-based engineered fluid (Novac 7000, 3M), which we adopted for its low boiling point at atmospheric conditions (34 °C at 1 atm), nonflammability, and low toxicity.^[46] This fluid is vaporized by a textile-based heater for pressurization and, conversely, at room temperature this fluid cools and condenses when the heater is turned off, allowing the pouch to deflate (**Figure 1A**). An internal textile sensor provides a pressure feedback signal, and a proportional-integral controller modulates the heating power to achieve continuous pressure command tracking, as opposed to binary actuation. A major advantage of this closed-loop pressure control is that it enables the soft robotic textiles to accurately actuate wearable devices that need to synergistically interact with the user or apply controlled forces amidst unpredictable thermal environments (**Figure 1B,C**). STATs are fabricated using a facile and highly customizable layered production process employing laser cutting and heat pressing equipment (**Figure 1E**), facilitating the production of arbitrarily complex systems such as multidimensional actuated textile arrays with independently programmable elements (**Figure 1F**) that can transform from planar sheets to 3D actuated textiles.

To achieve a highly customizable, scalable, and simple manufacturing process, fabrication of STATs is inspired by manufacturing paradigms that integrate sensing and actuation, such as those seen in pop-up MEMS^[47] and multimaterial 3D printing,^[48] but in this case applied to low-cost, textile-based materials. Unlike other textile-based robotic devices, which rely on either sewing^[32] or structural textile formation,^[33] STATs are formed using non-textile-specific equipment in a layered material deposition and removal approach, and unlike elastomeric phase change actuators,^[35] no one-off molds or wet-processing and curing times are required. Using our lamination-based automated process—reminiscent of integrated circuit fabrication—it is possible to precisely pattern and integrate the fully soft sensing and actuation components that are required for the implementation of closed-loop control using simple fabrication steps (**Figure 2**).

A heat-sealable textile forms the substrate for electrically active components (heater, sensor) while imparting vapor impermeability with its thermoplastic polyurethane (TPU) coating. Researchers have found that TPU has better impermeability to the Novac fluid than other elastomers.^[41] To make electronic components, we adhered a conductive textile to the substrate, used a laser to pattern the conductor, and subsequently removed excess material. The patterned conductive textile was permanently bonded to the substrate textile with heat and pressure, while reflow of TPU maintains vapor impermeability. By repeating the fabrication steps—i) temporary adhesion, ii) laser patterning, iii) removal, with additional conductive textile and thermal film layers added as needed, and iv) bonding—more complex electronic components, like sensors, can also be manufactured (**Figure 2A**). This scalable fabrication approach

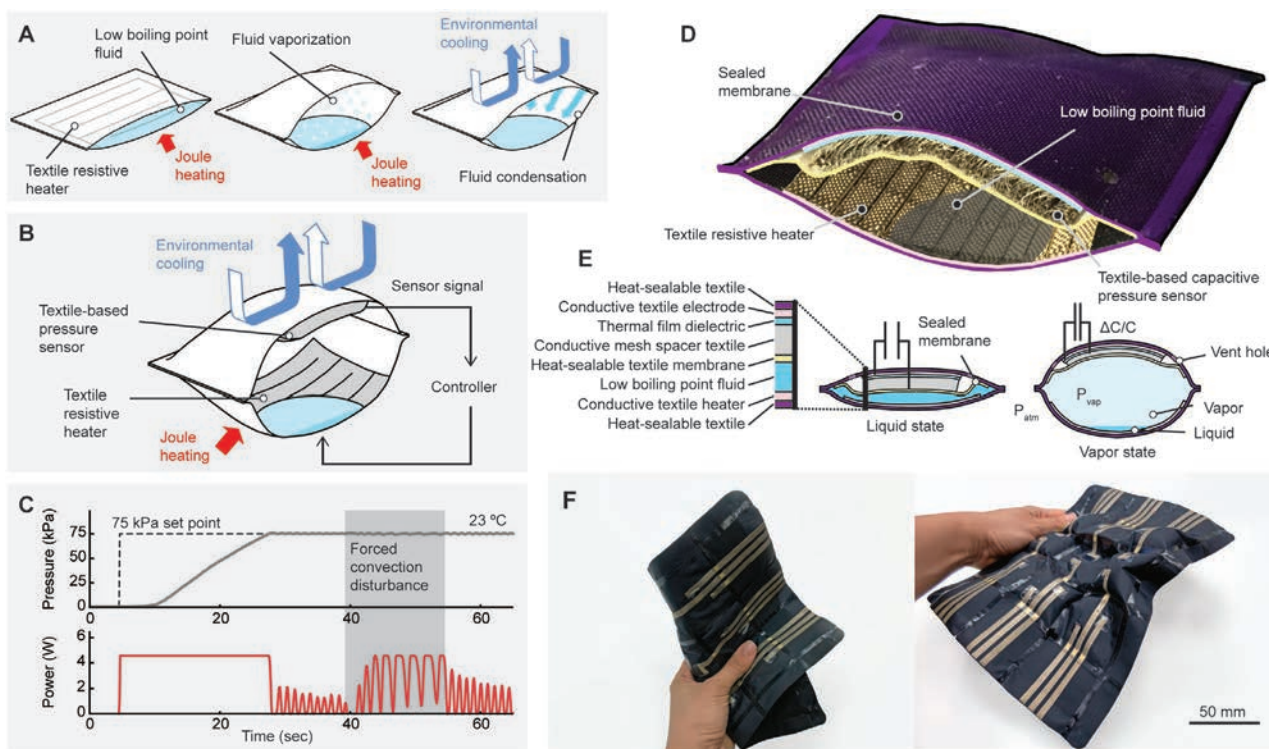


Figure 1. Overview of smart thermally actuating textiles (STATs). The basic mechanism of STATs operation is shown in (A), where an input of heat vaporizes a working fluid, which subsequently pressurizes the module. The implementation of (B) closed-loop control enables STATs modules to maintain internal pressures during environmental disturbances (for example, forced convection with 43 LPM airflow from a 50 mm distance shown in (C)). (D) A recolored photograph of a single 35×35 mm STAT module and (E) cross-section schematics at deflated and inflated states illustrate the functional materials that make up STATs, which can be implemented in connected arrays (3×3 array pictured in (F)).

enables the production of textile sheets with large numbers of identical—or distinct—arrays of STATs, formed by layering components with a heat-sealable textile membrane in-between and bonding at the edges (Figure 2B,C). Electrical connections made of conductive threads connect the heater and sensor electrodes to their respective power and signal lines (Figure 2C) and enable fully soft STATs. Detailed fabrication processes are provided in the Supporting Information.

3. STAT Characterization

With the goal of developing design guidelines for STATs, we studied the impact of a number of material and geometric parameters on peak pressure and the temporal pressure response. We characterized the fundamental pressure–temperature relationship between the fluid and the textile pouch and determined that the pressure–temperature relationship for the saturated fluid (Figure 3A) enables vapor pressures of a magnitude relevant to soft robotic garment applications (>50 kPa, as previously reported^[8]) at temperatures safe for wearable applications.^[49] Meanwhile, in contrast to the monotonic pressure–temperature relationship for Novec inside of a rigid vessel (Figure 3A), the inextensible yet flexible nature of STATs results in a unique physical behavior over two distinct regimes. Above the boiling point of Novec 7000, the internal pressure is dictated by the saturated Novec 7000 vapor as the textile walls prevent

expansion, in agreement with our fluid pressure–temperature model and experimental data observed in the rigid vessel. Below the boiling point, however, the textile walls don't provide the structural support required to allow subatmospheric pressure, and the internal pressure balances with external atmospheric pressure (a small amount of noncondensable gas left in the device from the filling process provides the excess pressure above that contributed by Novec 7000). Thus, below the boiling point of Novec, the STATs exhibit textile-like behavior where the internal pressure balances with atmospheric pressure and enables STATs to remain compliant and flexible, while above the boiling point the actuator-like behavior of STATs is captured by our thermofluidic model (detailed in the Supporting Information), which provides understanding—and design guidelines—for STATs and their controller.

We also studied the impact of STATs heater geometric design on manufacturing uniformity and heating distribution, as the fabrication method affords great controllability in patterning. Specifically, we characterized a range of textile heater designs in a fixed area by varying conduction path geometry in terms of path length and width (Figure S13, Supporting Information). The heaters of a fixed area all had material resistivities of $1.42 \times 10^{-5} \Omega \text{ m}$ (SD = $1.14 \times 10^{-6} \Omega \text{ m}$), yet their resistances spanned approximately two orders of magnitude (1.9–132.9 Ω) across different geometries. Lower resistance (and thus, for constant power, lower voltage) heater designs have better inter-sample resistance consistency (Figures S13 and S14, Supporting

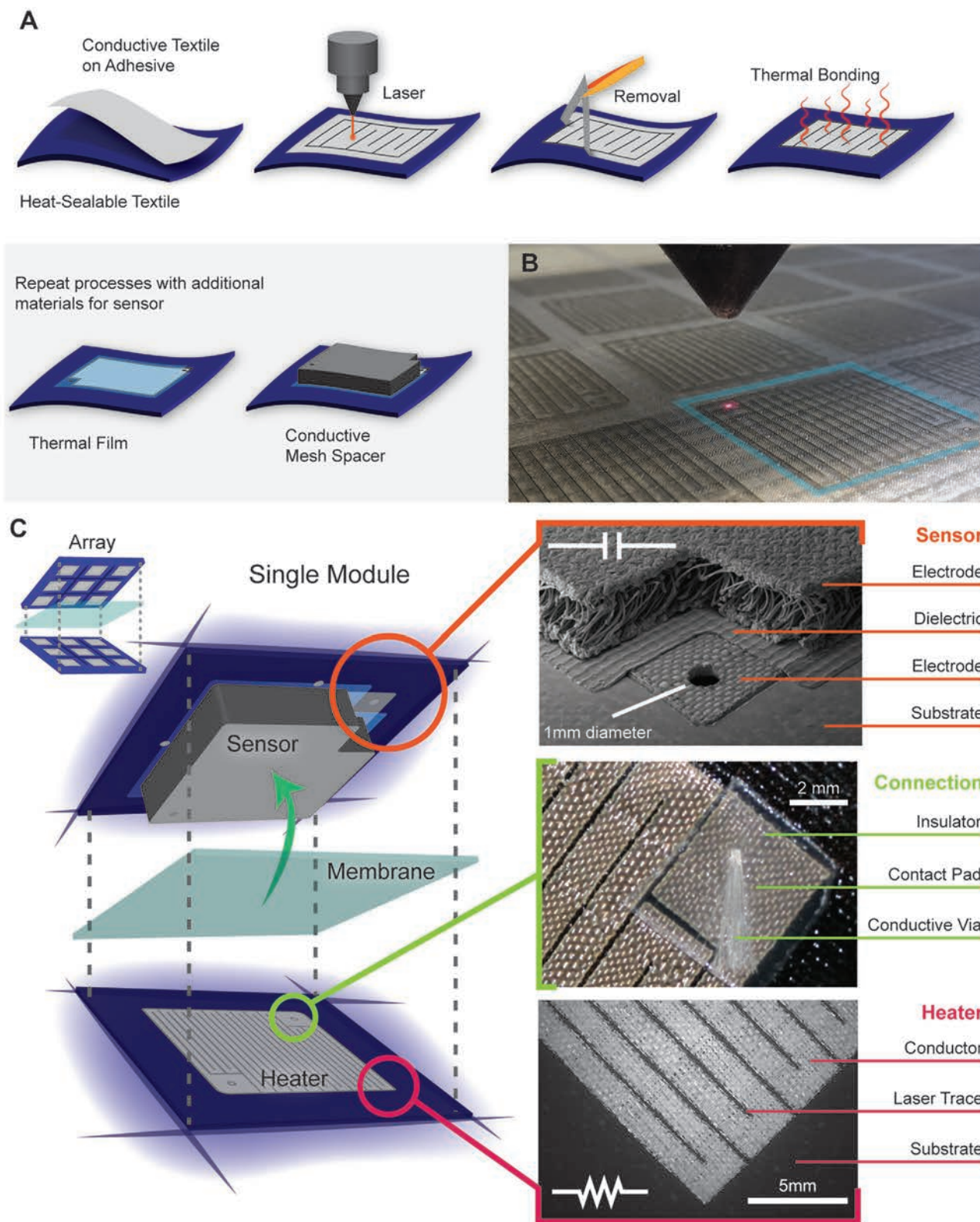


Figure 2. Fabrication of a STAT module. A) Laminated fabrication can form heaters and sensors, and (B) laser patterning can create multiple components in batches. C) Integrated modules are built by pairing heat sealable textiles and thermally bonding at edges and consist of (top) a capacitive sensor, (center) soft connections, and (bottom) Joule heaters.

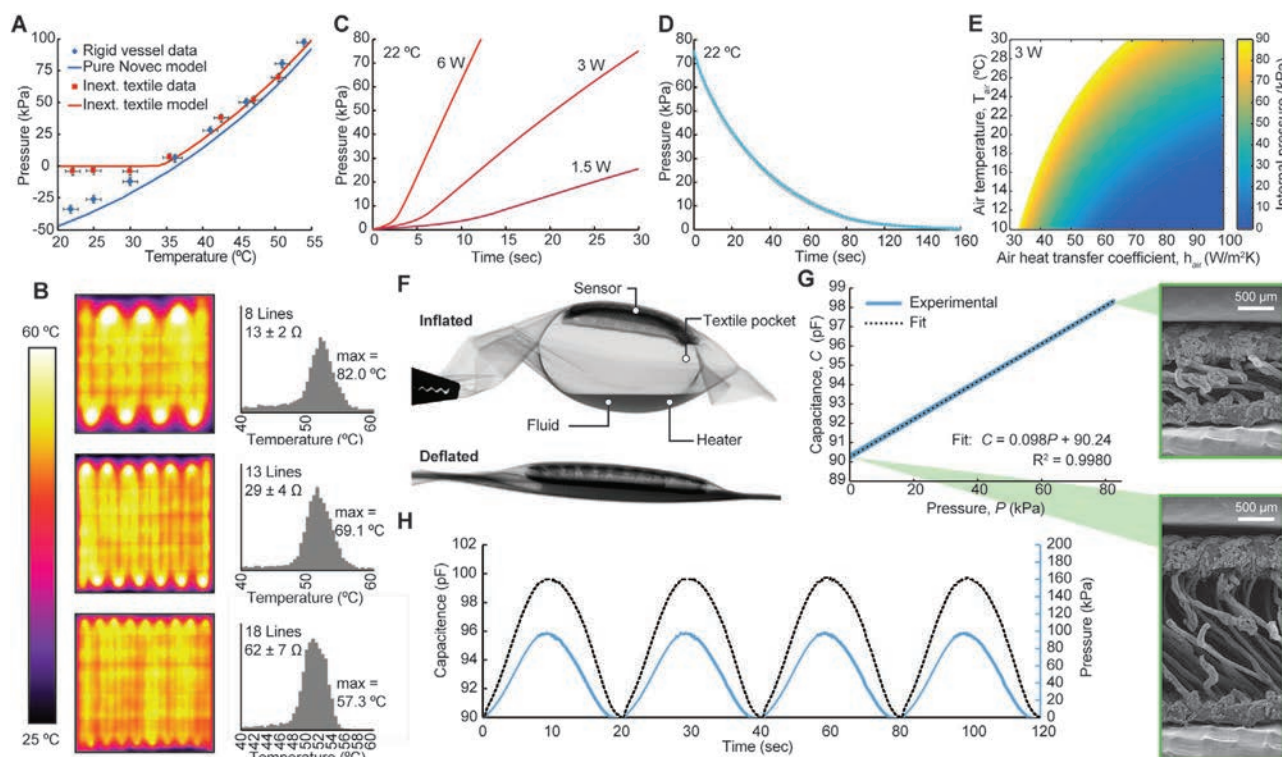


Figure 3. STAT characterization. A) We measured the steady-state pressure of Novec 7000 as a function of temperature within a STAT compared to a rigid container, which agreed well with our model. B) We took thermal images of three 25×25 mm heater designs at an average surface temperature of 50°C and plotted temperature distributions on histograms. We also studied the (C) open-loop pressurization of a STAT under three input powers at an environmental temperature of 22°C and (D) depressurization from 75 kPa due to ambient cooling at 22°C , based on seven heating and cooling cycles. E) The steady-state open-loop pressure response with a 3 W power input, as predicted from a thermal resistance network of a STAT (detailed in the Supporting Information), varies as a function of environmental conditions, motivating the need for closed-loop control. F) X-ray imaging shows both an inflated and deflated STAT. G) The capacitive textile pressure sensor responds linearly when subjected to air pressure from a regulator (10 pressurization cycles). SEM images on right are of sensor cross sections at two pressures highlighting the compressible, porous morphology of the mesh spacer textile. H) Four cycles of pressure sensor response illustrate repeatability.

Information), but exhibit a more heterogeneous temperature distribution due to less heat spreading through the underlying textile (Figure 3B),^[50] leading to a reliability tradeoff as hot spots form. Based on these findings, we optimized for this tradeoff by using heaters with between 11 and 15 lines in all experiments.

Given that STATs are manufacturable in arbitrary curved and rectilinear configurations, we developed an analytical model based on a thermal resistance network that accounted for conductive and convective pathways for heat transport within the system. This model enables us to understand the equilibrium pressurization behavior with varying airflow and temperature, described in detail in the Supporting Information text. We experimentally assessed the open-loop response of the actuators in 22°C , low-airflow environmental conditions to assess device performance and verify the analytical models using 35×35 mm STAT modules, chosen as a tradeoff between maximizing physical scale, enabling large strains during actuation, and minimizing response time (which relies on a high surface area to volume ratio because the heater is located on the interior pouch surface).

Pressurization response time of the actuators was demonstrated to be tunable based on the power input (Figure 3C), while the depressurization response times and profiles were shown to be consistent (Figure 3D). This consistency occurs

because depressurization is largely governed by free convective cooling to the environment driving condensation of the working fluid. The actuator required 140 s to fully depressurize from a peak pressure of 75 kPa at room temperature conditions, illustrating a limitation of all phase change actuation approaches in which the temporal response is dependent on the environment. Incorporation of active cooling elements, such as Peltier elements, could improve the response time in future implementations. In addition, our model predicted the open-loop response over a range of temperatures and airflow conditions using a thermal resistance network with a constant power input of 3 W (Figure S18, Supporting Information). This analysis revealed that temperature and airflow fluctuations on the scale of those encountered by people and their clothing have substantial consequences for the equilibrium pressure of the system and thus the pressurization response (Figure 3E).

To account for variation in environmental conditions, we implemented closed-loop feedback control by incorporating textile sensors for internal STAT pressure monitoring. We used a capacitive transduction mechanism with a conductive mesh spacer textile to realize the sensor. This enabled a repeatable linear response and increased sensitivity beyond that of similar sensors^[51] for operation in the pressure range of the actuators (Figure 3G,H). By using this sensor to obtain pressure

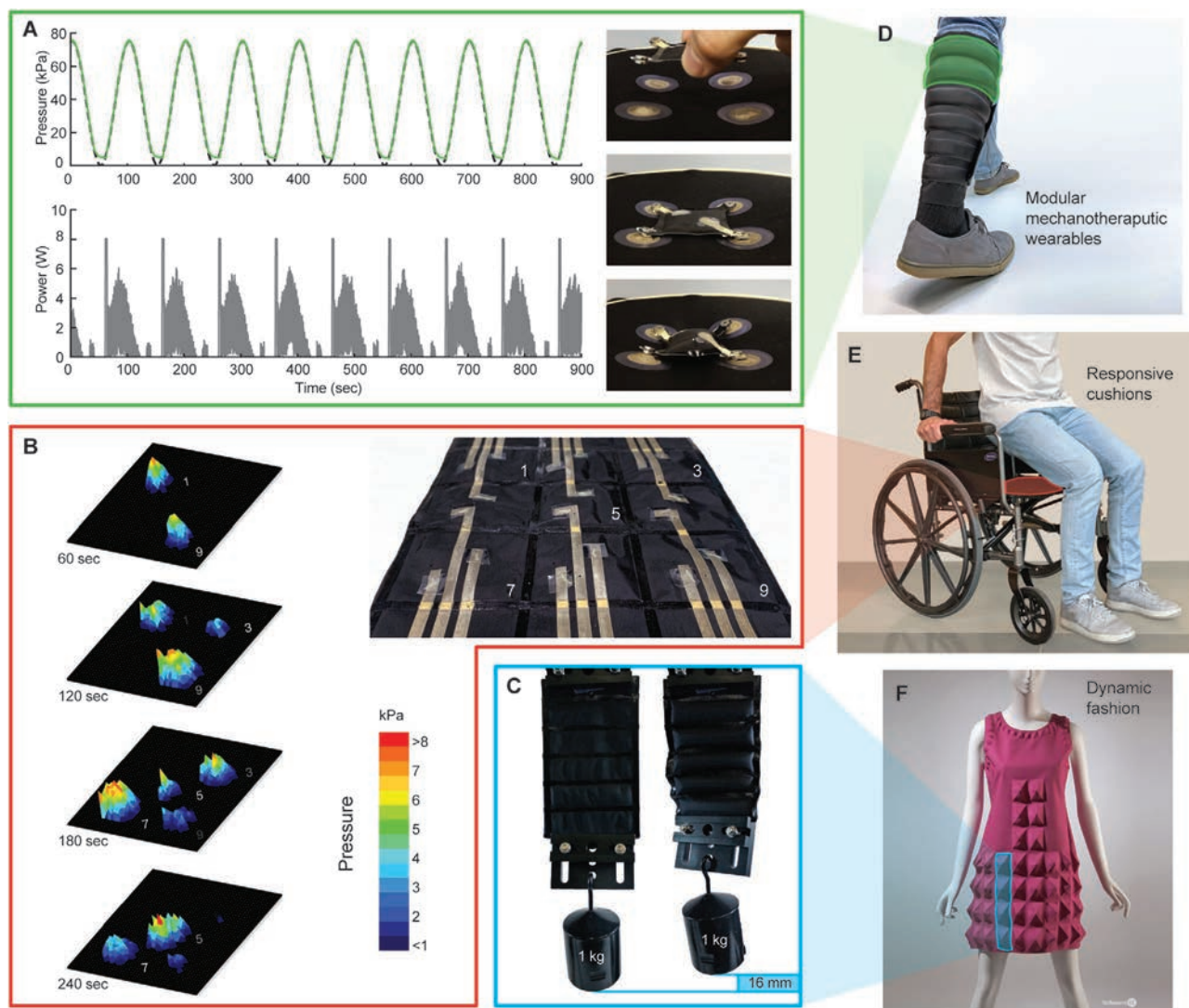


Figure 4. STAT demonstrations and applications. A) Left: We showed pressure tracking using closed-loop control, with the corresponding power input plotted of a single STAT. Right: Magnetic connections allow quick attachment and inflation, shown here before attachment, then in the unactuated and inflated states. B) We demonstrated temporal response of a 3×3 STAT array mat, which applied a pressure of up to 8 kPa on its environment when constrained in an enclosed space. C) Arrays of STATs can be formed in arbitrary configurations such as an artificial-muscle-like contracting actuator. The modularity of STATs can be used in devices like (D) customized, mobile mechanotherapeutic devices, while arrays can be incorporated as (E) dynamic wheelchair mats and even (F) fashion statements (inspiration pictured: Pierre Cardin dress, heat-molded Dynel, 1968 (photograph by Eileen Costa, The Museum at FIT, licensed under CC BY-SA 2.0)).

feedback and adjusting power to the heater through the use of a proportional-integral control system, STAT modules can accurately regulate pressure according to continuous input signals, including sine waves (Figure 4A). We also demonstrated controllability in different temperature environments (Figures S24 and S25, Supporting Information) and with temperature and airflow disturbances (Figure 1C, Movie S2, Supporting Information).

STATs are developed for wearable applications, so we characterized their durability when exposed to repeated washing, repeated bending, and extreme applied forces to provide insight into the STAT lifetime during scenarios potentially encountered in typical clothing use. Because STATs are built on a TPU-coated textile substrate, they have intrinsic water resistance, enabling

washability without degradation (Figure S20, Supporting Information). Due to the compliant and resilient nature of textile materials, STATs are robust and do not exhibit degradation after repeated bending and under extreme applied forces (Figures S21 and S22, Supporting Information).

4. STAT Demonstrations

We implemented STATs in several application areas. STAT devices with magnetic connection interfaces were fabricated to demonstrate how this soft robotic approach can allow modular, rapidly interchangeable, reconfigurable system designs (Figure 4A and Movie S2, Supporting Information). Furthermore,

we demonstrated arrays of multiple independently controllable STAT modules, which can be realized without the added bulk and weight of air lines and valves required in pneumatic devices (Figure 4B, right). These arrays are able to exert set pressures in a programmed manner upon their surroundings, even when constrained (i.e., actuating against a load) (Figure 4B, left, and Movie S3, Supporting Information). Additionally, we showed that arrays of STATs can be implemented in varied configurations because of their customizable manufacturing, such as lightweight artificial muscles (Figure 4C) inspired by Inflatable Servo Actuators.^[44] STAT-based soft robotic designs can also be implemented in wearable applications; for example, modular arrays can be implemented in mobile mechanotherapeutic devices (Figure 4D), where programmed pressure profiles delivered at personalized locations can improve healing.^[52–54] Connected STAT arrays can be used as cushions for wheelchair users (Figure 4E) in order to minimize pressure points and potentially prevent pressure sores.^[55] Finally, STATs have the potential to be designed into dynamic interpretations of fashion (Figure 4F) and potentially used in shape-changing clothing for thermal management^[56] and communication,^[57,58] where they could enable garments that can change length and incorporate unique, 3D shape changes to enable new approaches in these fields.

5. Conclusion

We have developed dynamically controllable, thermally actuating textile robots: STATs. STATs combine phase change actuation and textile materials which precludes the requirement for a pneumatic tether and will enable the development of compact wearable devices. Our scalable and accessible production approach enables high customizability and batch fabrication. We have studied the effects of environmental variability on STAT operation and implemented a closed-loop control approach to account for uncertainties, enabling STATs to be highly controllable and reprogrammable. We demonstrate the applicability of STATs with prototypes ranging from individual modular samples to connected arrays of varied geometries suitable for wearable use cases. In the future, we foresee inclusion of active cooling components or heat-pipe elements into the STAT design to enable faster and more precise deflation profiles; meanwhile, patterned incorporation of stretchable knit heat-sealable textiles, inspired by soft robotics work performed with elastomers,^[59] would enable more complex actuation profiles.

6. Experimental Section

SEM Imaging: SEM images were taken with a Tescan Vega GMU scanning electron microscope to capture the morphology of STAT components. Heater samples (Figure 2C, Figure S1, Supporting Information) were prepared by mounting samples to aluminum pin mounts with conductive carbon tape. Top view sensor samples (Figure 2C) were prepared by mounting to aluminum pin mounts with conductive carbon tape and sputter coating with gold. Cross-sectional sensor samples (Figure 3G) were mounted on an adjustable aluminum stage in uncompressed and compressed states, corresponding to a 10 pF capacitance change measured with a capacitance meter (Model 3000, GLK Instruments, USA), and sputter coated with gold.

Steady State Pressure–Temperature Characterization: Square-shaped actuator samples (45 mm × 45 mm) that did not incorporate integrated heaters or soft pressure sensors were prepared. These samples did incorporate an integrated 1/8" pneumatic line that was coupled to a capped one-way valve and a potted waterproofed pressure sensor (ADP5151, Panasonic; electrical connections embedded in Dragon Skin 10-NV silicone elastomer, Smooth-On, Inc.; (Figure S26, Supporting Information). The pressure sensor was monitored and recorded using a DAQ (USB-6218 BNC, National Instruments) and output to a computer.

The sample pockets were prefilled with 1.5 mL of Novec 7000 via syringe through the connected tubing to ensure excess fluid was present for venting, which was performed to remove noncondensable gas (i.e., air) from the system. To perform venting, the fluid-filled samples were submerged in a water bath heated to a temperature above the Novec boiling point (to between 40 and 45 °C). When the samples were pressurized to 10 kPa, the system was vented by uncapping the one-way valve, enabling some vaporized Novec along with noncondensable gases to escape to the environment, and recapping after 5 s. This venting process was repeated three times.

To collect the steady state pressure–temperature data, the prevented samples were submerged in a water bath (Isotemp Model 2228, Thermo Scientific) and mixed continuously (RW 20 Digital Overhead Stirrer, IKA) to provide a uniform water temperature. An external thermocouple was immersed in this water bath for temperature monitoring. When the temperature of the water bath stabilized, the entire system (sample, pneumatic line and pressure sensor) was immersed (Figure S26, Supporting Information). This system immersion prevented collection of condensate at the pressure sensor side of the STAT as might occur due to a water-air temperature gradient with an external sensor. The pressure of the system was recorded when it reached a steady state and plotted against the model in this paper (Figure 3A).

Resistive Heater Thermal Characterization: Heater samples were produced with several design parameters constrained to provide a general understanding of their thermal response. First, nonconducting regions of the heater were minimized by making cuts into the conductive textile the size of the ablation width of the laser beam (200 μm, Figure S1, Supporting Information). Second, a pattern where the pathway had a constant width (Figure S11, Supporting Information) was used. Third, the overall heater area was constrained to 25 mm × 25 mm squares (Figure S11A, Supporting Information). Each heater thus had a fixed square area and the heating pathway could be divided into N number of lines, where N is an integer. Square heater designs (25 mm × 25 mm) that represented a range of resistances ($N = 8$, $N = 13$, and $N = 18$) (seven samples for each condition) were thermally characterized with a constant input power (3 W) to allow comparison between heater path geometries. In order to maintain an equivalent power input, the voltage required to provide 3 W for each element was calculated based on the measured resistance of each sample using Ohm's law and the electrical power law.

A test rig (Figure S12A, Supporting Information) allowed measurements of surface temperature with a thermal imaging camera (T440, FLIR). The thermal imaging camera and textile heater samples were affixed to adjustable mounts that were in turn affixed to a linear rail. The camera had a laser guide that allowed the heater samples to be repeatedly aligned with the camera's optical axis through fiducial markers on the mount. To obtain an accurate estimation of the surface temperature, the samples were mounted facing away from the thermal imaging camera to avoid imaging artifacts due to the emissivity of the conductive textile material. An adjustable DC power supply (TP3005T, Tekpower) was used to supply the 3 W power input to each sample. A large venting feature on the sample mount provided a region for free convective heat transfer from the samples to the surrounding air. The entire rig was encapsulated in a shroud to prevent stray light from being captured by the thermal imaging camera. Thermal imaging software (ExaminIR Pro, FLIR) was used to capture the surface temperature data in real time. The emissivity of the black textile was approximated to be 0.95 and set in the FLIR software. A region of interest box of 97 × 97 pixels corresponding to the heater element area was digitally aligned with the sample (Figure S12B, Supporting Information).

Power was supplied for 6 s, and the spatial surface temperature at the region of interest logged at 30 Hz over this time period. Data was post-processed using the thermal imaging software. For each video frame, a mean temperature was based on the 9409 pixels captured within the digital region of interest. Repeating this process for each frame provided mean surface temperature with respect to time. To assess differences in spatial temperature distribution, still images were acquired for each design when the mean temperature over the 97×97 pixel digital region of interest reached $50\text{ }^{\circ}\text{C}$, and temperature values for each pixel were exported and histograms were generated for each design to illustrate differences in the temperature distribution (Figure 3B). Histograms were based on $0.5\text{ }^{\circ}\text{C}$ intervals across a temperature range of $40\text{--}60\text{ }^{\circ}\text{C}$.

Open-Loop Pressure Response Characterization: A 13-line heater design was used for these studies as a compromise between robustness and the ability to deliver relatively high powers ($\approx 6\text{ W}$) at relatively low voltages ($<15\text{ V}$). $35 \times 35\text{ mm}$ pouches were fabricated by laminating an additional woven textile layer to a heater textile layer. Each pouch incorporated a short pneumatic line tether that was connected to a pressure sensor (NSCDANN015PAUNV, Honeywell) to assess the internal actuator pressure. An instrumentation amplifier (UV series, Honeywell) was used to amplify the pressure readout and provide an analog signal. This analog signal was acquired by an analog-to-digital data acquisition system (Powerlab, AD instruments) and logged in Labchart (AD instruments) at a rate of 1 kHz.

The effect of power input on response time was characterized first (Figure 3C). A sealed heater sample was mounted horizontally such that the heater was facing upward with the fluid resting in direct contact. A volume of 0.5 mL of Novec 7000 fluid was injected into the pouch using a syringe before being coupled to the pressure sensor, with negligible remaining air inside the pouch. The pouch was actuated at 1.5, 3, and 6 W for 30 s, but if the internal actuator pressure reached 80 kPa, power was set to zero to prevent rupture. The power supply voltage was set according to the desired power and baseline voltage of the sample, as calculated using Ohm's law and the electrical power law. The experiment was performed at room temperature ($22\text{ }^{\circ}\text{C}$), and the temperature was monitored throughout using a thermometer to ensure consistency. The experiment was repeated seven times for each condition and transient profiles based on the mean of all individual profiles were generated. The depressurization rates of actuators were assessed during these tests (Figure 3D). Devices were pressurized in excess of 75 kPa before the input power was removed and the pressure profile captured until the actuator reached 0 kPa. Cooling profiles initiating from the 75 kPa point were then temporally aligned to allow comparisons between actuation cycles. A mean depressurization profile was captured based on the average of seven runs.

X-Ray Imaging: For the X-ray images in Figure 3F, a $45 \times 45\text{ mm}$ module was fabricated with an integrated heater and sensor. 0.5 mL of fluid was injected via syringe and the module was sealed with instant adhesive. X-ray transmission images at an uninflated state and inflated state were acquired with a micro-CT system (XRA-002, X-Tek).

Sensor Characterization: A $35 \times 35\text{ mm}$ pouch with an integrated soft pressure sensor and no heater was thermally sealed and a pneumatic line was bonded to the module for external inflation. The sample was connected to a test rig (Figure S27, Supporting Information) where the sample was gradually pressurized using an electro-pneumatic regulator (ITV1011-21N2BL4, SMC corporation) which was in turn controlled by a real-time control system (cRIO 9030, National Instruments). The controller provided a sinusoidal input to the regulator at a frequency of 0.05 Hz and set-point amplitude of 0–100 kPa. The electro-pneumatic regulator output inflated the sample and a commercially available pressure sensor (NSCDANN015PAUNV, Honeywell) instantaneously measured the pressure. An instrumentation amplifier (UV series, Honeywell) was used to amplify the commercial pressure sensor line and provided an analog signal. An air reservoir (9166, Firestone Industrial Products) increased the overall volume of air being pressurized to minimize overshooting from the air regulator controller, ensuring smooth pressurization of the sample. A capacitance meter (Model 3000, GLK Instruments) was connected to the sample's sensor terminals to measure capacitance during pressurization. Analog voltages relating the

capacitance and pressure signals were acquired by an analog-to-digital data acquisition system (Powerlab, AD instruments) and logged in Labchart (AD Instruments). Data were captured at 1 kHz.

All pressure sensors were calibrated by pressurizing and depressurizing the sensors for 10 cycles. For each of the ten pressurization phases, a linear regression was calculated using the least squares method and then all lines-of-best-fit were subsequently averaged to determine sensor sensitivity (0.098 pF kPa^{-1} ($R^2 = 0.998$) in Figure 3G). A sensor was repeatedly pressurized and depressurized a total of 200 consecutive cycles to determine the repeatability (Figure 3H).

Closed-Loop Controller: The STAT module was integrated with a real-time control system (cRIO 9030, National Instruments) to enable closed-loop control (Figure 4A). The capacitive textile sensor terminals were connected to a capacitance meter (Model 3000, GLK Instruments) which provided a real-time voltage output based on the instantaneous capacitance of the sensor. This signal is read by the real-time controller via an analog input module (NI 9205, National Instruments) which converts the signal to a digitized format which is implemented on a field-programmable gate array (FPGA). This sensor data (digitized voltage values) were converted to the digitized pressure values based on the sensor calibration procedure. This pressure information provided the feedback information for a proportional-integral (PI) control block implemented on the FPGA. A commanded pressure input can be supplied to the PI control block via a host PC (as a manually controlled step input), or a signal generator can be used to provide a dynamically varying input to be implemented on the real-time controller of the cRIO. This signal generator could provide step, triangular, or sinusoidal inputs to the PI control block. The proportional gain was set to 0.8 and the integral gain set to 1.0 based on empirical tuning. The output from the PI controller was converted to an analog output signal via an analog voltage output module on the cRIO (NI 9264, National Instruments). This voltage output was then fed to a linear electrical power amplifier which can supply up to 10.3 W of continuous power at a peak of 12 V.

Environmental Disturbance Experiment: A 15-line modular STAT with fastener-based heater connections and soft sensor connections was fabricated using the patterns in Figures S2 and S3 (Supporting Information). The sensor was pre-calibrated and the STAT was mounted to a base textile dock with magnetic connectors at sensor lines. This experiment was performed under a consistent temperature of $23\text{ }^{\circ}\text{C}$. For the disturbance, an air tube was positioned 50 mm away from the STAT, where the tube's airflow rate was 43 liters-per-minute. The flow rate was pre-calibrated by measuring the volumetric displacement of fluid following a procedure described in the literature.^[60] The previously described closed-loop control system controlled the STAT.

Using the controller allowed the STAT to equilibrate to a set pressure of 75 kPa for several seconds, with airflow off. The tube airflow was subsequently switched on for several seconds and then turned back off. The internal pressure and power data were logged during the experiment (Figure 1C), and an overhead thermal camera captured the temporal temperature distribution of the STAT.

Modular STAT Demonstration: A modular STAT with soft connectors in the geometries of Figures S2 and S3 (Supporting Information) and a base textile dock were fabricated (Figure S5, Supporting Information). A total of 0.5 mL of Novec 7000 was injected into the sample, and the sample was then sealed with a minimal amount of residual air. The controller was programmed to a set pressure of 75 kPa or a 75 kPa sinusoidal waveform input (Movie S2, Supporting Information). The module was dropped onto the base textile dock to track the preset input pressure.

STAT Array Demonstration: A connected 3×3 array of nine individual STAT modules incorporating 15-line heaters, textile-based pressure sensors, and integrated sensor signal lines was fabricated based on the geometries in Figures S6 and S7 (Supporting Information), and each module was filled with 0.7 mL of Novec fluid.

Due to the electronic hardware requirements of controlling nine actuators at once, the array demonstration implemented a different controller than then the single STAT control experiments as illustrated in Figure S28 (Supporting Information). The array was controlled via a real-time control system (Simulink 6.6, Mathworks) to enable closed-loop

control. The capacitance-based textile sensor terminals were each connected to a capacitance-to-digital converter IC (FDC2214-Q1, Texas Instruments) input channel, which sent a digital signal corresponding to the instantaneous capacitance of each module in the array over i2c to a microcontroller, (Arduino Nano, Arduino). The capacitance readings were analyzed in software and sent out as a PWM signal to a low-pass filter bank for conversion to an analog signal. This analog signal, which is directly proportional to the pressure inside of each textile module, was read in by the real-time controller via an analog input/output module (PCI-6259, National Instruments). Depending on the desired actuation profile of the array, a commanded pressure input waveform was supplied to a PI control block via the target computer. The proportional gain was set to 150 and the integral to 500 based on empirical tuning. The output of the PI controller block was converted to an analog output between 0 and 5 V via an analog output device (PCI-6733, National Instruments) and fed to a DC motor driver (950 Series, Moticont). The driver output was connected to the corresponding heater lines of the actuators on the array.

To achieve the actuation patterns seen in Movie S3 (Supporting Information), the STAT array was programmed to first actuate sequentially and then subsequently in a cross pattern. These actuation profiles were performed in constrained and unconstrained environments. The constrained experiments used a custom mount blocked with an acrylic plate and a pressure sensor mat (I-Scan, Tekscan) such that the actuators apply force on the plate. The mount had 17.5 mm of free space between the bottom of the acrylic plate and the STAT array sample, which was filled partially with 10 mm open cell foam for pressure sensor mat readout (Figure S24, Supporting Information). In this experiment, all actuation occurred in a sinusoidal actuation profile with a frequency of 0.003 Hz and an amplitude between 0 and 60 kPa. In the constrained actuation profile (Figure 4B, Movie S3, Supporting Information), only the first, third, fifth, seventh, and ninth actuators were commanded to actuate, each with the same 60 kPa and 0.003 Hz sine wave, but the five actuators had a phase lag of 36°, with the fifth (middle) actuator inflating last. For the unconstrained actuation condition (Movie S3, Supporting Information), where each actuator is actuated sequentially, the acrylic plate and the pressure sensor mat were removed and an IR time of flight camera (CamBoard pico flex, PMD Technologies) captured relative displacement. The first module to be actuated had a 20° phase shift, the second had a 40° phase shift, etc., until the ninth actuator which had a 180° shift. For all experiments, the internal pressure data were logged directly in Simulink by the target computer.

Artificial Muscle Demonstration: A 5 × 1 STAT array was fabricated in the pattern geometry shown in Figure S8 (Supporting Information) and a 1 kg weight was attached to a fixture mechanically clamped to the lower edge of the array. The actuator was inflated at 6 W for 30 s, allowing it to contract, and the peak displacement was obtained from a video still (Figure 4C).

Image Preparation: Several images were edited with Adobe Photoshop and Adobe Illustrator software to improve clarity. Figure 1D had the background removed, was recolored for easy differentiation of the layers, and had a color added to simulate the fluid which could not be captured in a cross-sectional photograph. Figures 1F, 3F, and 4B,C had the backgrounds removed. Additionally, Figure 4C was corrected for camera lens distortion to enable recording of accurate measurements. Figure 4D,E had the backgrounds recolored and brand logos on shoes blurred. Image 4F had the background expanded.

The volunteers taking part in the photos, depicted in Figure 4, have consented to the photos being taken and their inclusion in the publication.

Supporting Information

Supporting Information is available from the Wiley Online Library or from the author.

Acknowledgements

This research was partly funded by the National Science Foundation EFRI, Award (No. 1830896), NSF MRSEC award DMR-1420570, the Wyss

Institute for Biologically Inspired Engineering and the Harvard John A. Paulson School of Engineering and Applied Sciences. V.S. acknowledges the support of the United States Department of Defense through the National Defense Science & Engineering Graduate (NDSEG) Fellowship Program and the National GEM Consortium through the GEM Fellowship. The authors would like to thank Ozgur Atalay for discussions and Max Rousseau for fabrication videography.

Conflict of Interest

George Whitesides acknowledges an equity interest and board position in Soft Robotics, Inc.

Author Contributions

V.S. and C.J.P. contributed equally to this work. V.S., C.J.P., A.T.A., M.B., and C.J.W. conceived the work. V.S., C.J.P., D.J.P., and J.T.A. designed and fabricated the devices. V.S., C.J.P., D.J.P., J.T.A., J.C.W., and D.M.V. performed the experiments and analysis. V.S. and D.J.P. developed the models. V.S., C.J.W., R.J.W., and G.M.W. oversaw the work.

Keywords

phase change actuators, robotic textiles, soft actuators, soft devices, soft sensors

Received: April 22, 2020
Revised: May 18, 2020
Published online: July 2, 2020

- [1] C. Laschi, B. Mazzolai, M. Cianchetti, *Sci. Rob.* **2016**, *1*, eaah3690.
- [2] D. Rus, M. T. Tolley, *Nature* **2015**, *521*, 467.
- [3] R. F. Shepherd, F. Ilievski, W. Choi, S. A. Morin, A. A. Stokes, A. D. Mazzeo, X. Chen, M. Wang, G. M. Whitesides, *Proc. Natl. Acad. Sci. USA* **2011**, *108*, 20400.
- [4] E. T. Roche, R. Wohlfarth, J. T. B. Overvelde, N. V. Vasilyev, F. A. Pigula, D. J. Mooney, K. Bertoldi, C. J. Walsh, *Adv. Mater.* **2014**, *26*, 1200.
- [5] L. N. Awad, J. Bae, K. O'Donnell, S. M. M. De Rossi, K. Hendron, L. H. Slood, P. Kudzia, S. Allen, K. G. Holt, T. D. Ellis, C. J. Walsh, *Sci. Transl. Med.* **2017**, *9*, eaai9084.
- [6] P. Polygerinos, Z. Wang, K. C. Galloway, R. J. Wood, C. J. Walsh, *Rob. Auton. Syst.* **2015**, *73*, 135.
- [7] C. T. O'Neill, N. S. Phipps, L. Cappello, S. Paganoni, C. J. Walsh, *Int. Conf. Rehabil. Rob.* **2017**, *2017*, 1672.
- [8] C. J. Payne, E. G. Hevia, N. Phipps, A. Atalay, O. Atalay, B. R. Seo, D. J. Mooney, C. J. Walsh, *IEEE Int. Conf. Rob. Autom.* **2018**, *2018*, 5459.
- [9] W. M. Huang, Z. Ding, C. C. Wang, J. Wei, Y. Zhao, H. Purnawali, *Mater. Today* **2010**, *13*, 54.
- [10] A. Lendlein, S. Kelch, *Angew. Chem., Int. Ed.* **2002**, *41*, 2034.
- [11] E. Edqvist, E. Hedlund, B. Lundberg, *Sens. Actuators, A.* **2010**, *157*, 198.
- [12] A. O'Halloran, F. O'Malley, P. McHugh, *J. Appl. Phys.* **2008**, *104*, 071101.
- [13] E. Acome, S. K. Mitchell, T. G. Morrissey, M. B. Emmett, C. Benjamin, M. King, M. Radakovitz, C. Keplinger, *Science* **2018**, *359*, 61.
- [14] V. Cacucciolo, J. Shintake, Y. Kuwajima, S. Maeda, D. Floreano, H. Shea, *Nature* **2019**, *572*, 516.

- [15] H. Nabae, A. Kodaira, T. Horiuchi, K. Asaka, G. Endo, K. Suzumori, *IEEE Int. Conf. Intell. Rob. Syst.* **2019**, 8287.
- [16] X. Yu, Z. Xie, Y. Yu, J. Lee, A. Vazquez-Guardado, H. Luan, J. Ruban, X. Ning, A. Akhtar, D. Li, B. Ji, Y. Liu, R. Sun, J. Cao, Q. Huo, Y. Zhong, C. M. Lee, S. Y. Kim, P. Gutruf, C. Zhang, Y. Xue, Q. Guo, A. Chempakasseril, P. Tian, W. Lu, J. Y. Jeong, Y. J. Yu, J. Cornman, C. S. Tan, B. H. Kim, K. H. Lee, X. Feng, Y. Huang, J. A. Rogers, *Nature* **2019**, 575, 473.
- [17] L. M. Castano, A. B. Flatau, *Smart Mater. Struct.* **2014**, 23, 053001.
- [18] T. L. Buckner, R. Kramer-Bottiglio, *Multifunct. Mater.* **2018**, 1, 012001.
- [19] M. C. Yuen, R. A. Bilodeau, R. K. Kramer, *IEEE Rob. Autom. Lett.* **2016**, 1, 708.
- [20] R. Granberry, K. Eschen, B. Holschuh, J. Abel, *Adv. Mater. Technol.* **2019**, 4, 1900548.
- [21] C. S. Haines, M. D. Lima, N. Li, G. M. Spinks, J. Foroughi, J. D. W. Madden, S. H. Kim, S. Fang, M. Jung de Andrade, F. Göktepe, Ö. Göktepe, S. M. Mirvakili, S. Naficy, X. Lepró, J. Oh, M. E. Kozlov, S. J. Kim, X. Xu, B. J. Swedlove, G. G. Wallace, R. H. Baughman, *Science* **2014**, 343, 868.
- [22] M. Kanik, S. Orguc, G. Varnavides, J. Kim, T. Benavides, D. Gonzalez, T. Akintilo, C. C. Tasan, A. P. Chandrakasan, Y. Fink, P. Anikeeva, *Science* **2019**, 365, 145.
- [23] A. Maziz, A. Concas, A. Khaldi, J. Stålhånd, N.-K. Persson, E. W. H. Jager, *Sci. Adv.* **2017**, 3, e1600327.
- [24] A. Frutiger, J. T. Muth, D. M. Vogt, Y. Mengüç, A. Campo, A. D. Valentine, C. J. Walsh, J. A. Lewis, *Adv. Mater.* **2015**, 27, 2440.
- [25] J. Lee, H. Kwon, J. Seo, S. Shin, J. H. Koo, C. Pang, S. Son, J. H. Kim, Y. H. Jang, D. E. Kim, T. Lee, *Adv. Mater.* **2015**, 27, 2433.
- [26] C. B. Cooper, K. Arutselvan, Y. Liu, D. Armstrong, Y. Lin, M. R. Khan, J. Genzer, M. D. Dickey, *Adv. Funct. Mater.* **2017**, 27, 1605630.
- [27] C. Mattmann, F. Clemens, G. Tröster, *Sensors* **2008**, 8, 3719.
- [28] S. Ryu, P. Lee, J. B. Chou, R. Xu, R. Zhao, A. J. Hart, S. G. Kim, *ACS Nano* **2015**, 9, 5929.
- [29] Y. Cheng, R. Wang, J. Sun, L. Gao, *Adv. Mater.* **2015**, 27, 7365.
- [30] C. K. Harnett, H. Zhao, R. F. Shepherd, *Adv. Mater. Technol.* **2017**, 2, 1700087.
- [31] X. Yang, Z. Chen, C. S. M. Elvin, L. H. Y. Janice, S. H. Ng, J. T. Teo, R. Wu, *IEEE Sens. J.* **2015**, 15, 757.
- [32] M. Yuen, A. Cherian, J. C. Case, J. Seipel, R. K. Kramer, *IEEE Int. Conf. Intell. Rob. Syst.* **2014**, 580.
- [33] J. Foroughi, G. M. Spinks, S. Aziz, A. Mirabedini, A. Jeiranikhameh, G. G. Wallace, M. E. Kozlov, R. H. Baughman, *ACS Nano* **2016**, 10, 9129.
- [34] A. Kaspar, L. Makatura, W. Matusik, in *Proc. 32nd Annu. ACM Symp. User Interface Softw. Technol.*, ACM, New Orleans, LA, USA **2019**, p. 53.
- [35] A. Miriyev, K. Stack, H. Lipson, *Nat. Commun.* **2017**, 8, 596.
- [36] M. Boyvat, D. M. Vogt, R. J. Wood, *Adv. Mater. Technol.* **2019**, 4, 1800381.
- [37] K. Nakahara, K. Narumi, R. Niiyama, Y. Kawahara, *IEEE Int. Conf. Rob. Autom.* **2017**, 2017, 1856.
- [38] R. Altmüller, R. Schwödiauer, R. Kaltseis, S. Bauer, I. M. Graz, *Appl. Phys. A* **2011**, 105, 1.
- [39] K. Narumi, H. Sato, K. Nakahara, Y. Seong, K. Morinaga, Y. Kakehi, R. Niiyama, Y. Kawahara, *IEEE Rob. Autom. Lett.* **2020**, 5, 3915.
- [40] Y. Nishikawa, M. Matsumoto, *Adv. Rob.* **2019**, 33, 567.
- [41] M. Garrad, G. Soter, A. T. Conn, H. Hauser, J. Rossiter, *RoboSoft 2019 – 2019 IEEE Int. Conf. Soft Robot.* **2019**, 74.
- [42] T. Noguchi, F. Tsumori, *Jpn. J. Appl. Phys.* **2020**, 59, S11L08.
- [43] M. Cartolano, B. Xia, A. Miriyev, H. Lipson, *Actuators* **2019**, 8, 9.
- [44] A. R. Mettam, Inflatable servo actuators, Ministry of Aviation, Royal Aircraft Establishment, RAE Farnborough **1962**.
- [45] R. Niiyama, X. Sun, C. Sung, B. An, D. Rus, S. Kim, *Soft Rob.* **2015**, 2, 59.
- [46] 3M Electronics Market Material Division, Product Information: 3M Novoc 7000 Engineered Fluid, **2009**.
- [47] J. P. Whitney, P. S. Sreetharan, K. Y. Ma, R. J. Wood, *J. Micromech. Microeng.* **2011**, 21, 115021.
- [48] R. L. Truby, M. Wehner, A. K. Grosskopf, D. M. Vogt, S. G. M. Uzel, R. J. Wood, J. A. Lewis, *Adv. Mater.* **2018**, 30, 1706383.
- [49] A. R. Moritz, F. C. Henriques, *Am. J. Pathol.* **1947**, 23, 695.
- [50] K. R. Bagnall, Y. S. Muzychka, E. N. Wang, *IEEE Trans. Compon., Packag., Manuf. Technol.* **2014**, 4, 408.
- [51] A. Atalay, V. Sanchez, O. Atalay, D. M. Vogt, F. Haufe, R. J. Wood, C. J. Walsh, *Adv. Mater. Technol.* **2017**, 2, 1700136.
- [52] C. J. Payne, I. Wamala, D. Bautista-Salinas, M. Saeed, D. Van Story, T. Thalhofer, M. A. Horvath, C. Abah, P. J. del Nido, C. J. Walsh, N. V. Vasilyev, *Sci. Rob.* **2017**, 2, eaan6736.
- [53] M. T. Loghmani, M. Whitted, *J. Physiother. Phys. Rehabil.* **2016**, 1, 1000122.
- [54] D. J. Preston, H. J. Jiang, V. Sanchez, P. Rothemund, J. Rawson, M. P. Nemitz, W. K. Lee, Z. Suo, C. J. Walsh, G. M. Whitesides, *Sci. Rob.* **2019**, 4, eaaw5496.
- [55] M. W. Ferguson-Pell, I. C. Wilkie, J. B. Reswick, J. C. Barbenel, *Paraplegia* **1980**, 18, 42.
- [56] X. A. Zhang, S. Yu, B. Xu, M. Li, Z. Peng, Y. Wang, S. Deng, X. Wu, Z. Wu, M. Ouyang, Y. H. Wang, *Science* **2019**, 363, 619.
- [57] H. P. Profita, N. Farrow, N. Correll, in *Proc. 9th Int. Conf. Tangible, Embed. Embodied Interact.*, Association for Computing Machinery, New York **2015**, p. 359.
- [58] F. Davis, A. Roseway, E. Carroll, M. Czerwinski, in *Proc. 7th Int. Conf. Tangible, Embed. Embodied Interact. – TEI '13*, Association for Computing Machinery, New York **2013**, p. 99.
- [59] J. H. Pikul, S. Li, H. Bai, R. T. Hanlon, I. Cohen, R. F. Shepherd, *Science* **2017**, 358, 210.
- [60] D. J. Preston, P. Rothemund, H. J. Jiang, M. P. Nemitz, J. Rawson, Z. Suo, G. M. Whitesides, *Proc. Natl. Acad. Sci. USA* **2019**, 116, 7750.